



# Modulating the anchoring states of Ag on TiO<sub>2</sub> by SiO<sub>2</sub> to boost the NH<sub>3</sub>-SCO activity over Ag-based catalysts

Chunxue Wang<sup>a,1</sup>, Zhao Li<sup>a,1</sup>, Xin Sun<sup>a,b</sup>, Yuan Li<sup>a,b</sup>, Lei Shi<sup>a,b</sup>, Shunzheng Zhao<sup>c</sup>, Kai Li<sup>a,b,\*</sup>, Ping Ning<sup>a,b,\*</sup>, Fei Wang<sup>a,b,\*</sup>

<sup>a</sup> Faculty of Environmental Science and Engineering, Kunming University of Science and Technology, Kunming 650500, China

<sup>b</sup> National Regional Engineering Center for Recovery of Waste Gases from Metallurgical and Chemical Industries, Kunming 650500, China

<sup>c</sup> School of Energy and Environmental Engineering, University of Science and Technology Beijing, Beijing 100083, China

## ARTICLE INFO

### Keywords:

Anchoring states  
Anchoring site  
Anchoring strength  
Ag-based catalyst  
NH<sub>3</sub>-SCO

## ABSTRACT

Ag-based catalysts show high activity in NH<sub>3</sub>-selective catalytic oxidation (NH<sub>3</sub>-SCO). The anchoring states of Ag species determines its valence and dispersion, thereby influencing the performance of Ag-based catalysts. Herein, we elucidated that the content and anchoring strength of the hydroxyl (OH) groups on support together affect the anchoring states of Ag. TiO<sub>2</sub> has few OH groups but high anchoring strength, the anchored Ag is in a highly dispersed oxidized state, while the unanchored Ag is aggregated in a metallic state (Ag<sup>0</sup>), so it presents an unevenly sized dispersion and mainly in oxidized state. SiO<sub>2</sub> has abundant OH groups but weak anchoring, and can excessively agglomerate into large Ag<sup>0</sup> nanoparticles (Ag<sup>0</sup> NPs). Therefore, the introduction of SiO<sub>2</sub> can regulate the anchoring states of Ag on the TiO<sub>2</sub> support, making Ag presents highly dispersed Ag<sup>0</sup> NPs, thus following a reaction mechanism with lower energy barriers and significantly improving the NH<sub>3</sub>-SCO performance.

## 1. Introduction

Ammonia (NH<sub>3</sub>), as a gaseous pollutant with strong pungent odor, mainly originates from human activities including industrial production, agriculture and vehicle exhaust [1,2]. The excess emission of NH<sub>3</sub> has a serious corrosive effect on human skin and respiratory tract [3,4]. NH<sub>3</sub> is the predominant alkaline pollutant and easily reacts with the acidic gases (e.g., NO<sub>x</sub> and SO<sub>2</sub>) to form secondary inorganic aerosols (e.g., (NH<sub>4</sub>)<sub>2</sub>SO<sub>4</sub> and NH<sub>4</sub>NO<sub>3</sub>), which account for 20–80 % of total PM<sub>2.5</sub> [5,6]. In addition, under the context of the “dual carbon” target, zero-carbon fuels (e.g., NH<sub>3</sub>/H<sub>2</sub> or H<sub>2</sub>) are currently on the rise in energy field [7,8]. The slipping and incomplete combustion of NH<sub>3</sub> have brought the NH<sub>3</sub> abatement and effective control back into the general public's view, attracting extensive attention from researchers.

To date, compared with other technologies (such as absorption, biological conversion, and thermal combustion), the NH<sub>3</sub>-SCO is considered the most promising process for application due to high efficiency [9]. Noble metals, transition-metal oxides, and metal-modified Zeolites are the primary types of NH<sub>3</sub>-SCO catalysts. Noble metal catalysts (Pt, Pd, Au, and Ir) usually exhibit excellent low-temperature

oxidation activity, however, accompanied with low N<sub>2</sub> selectivity due to over-oxidation of NH<sub>3</sub> [10,11]. Although transition-metal oxides, and metal-modified Zeolites possess low cost and high N<sub>2</sub> selectivity in NH<sub>3</sub>-SCO, their higher temperature window limits their widespread application [12–15]. Ag-based catalysts have been extensively investigated in recent years, which can give consideration to both superior activity and low cost [16–19]. Previous studies revealed that Ag<sup>0</sup> is the mainly active species in NH<sub>3</sub>-SCO reaction at low temperature, and more well-dispersed Ag<sup>0</sup> NPs are favored for improved activity [20,21]. It has been reported that Ag species usually tended to existed on SiO<sub>2</sub> in the form of Ag<sup>0</sup> NPs [22–24], but its exact mechanism remains unclear. However, the formation of Ag<sup>0</sup> NPs on SiO<sub>2</sub> is not always favor for the NH<sub>3</sub>-SCO activity due to the decrease in exposed active sites result from excessive aggregation [22]. As well known, both the dispersion and the valence state of Ag species on Ag-based catalysts are related to their anchoring states on the support. Investigating the intrinsic factor for determining the anchoring states of Ag species, and reasonably modulating the anchoring states are of great significance for the synthesis of highly active NH<sub>3</sub>-SCO catalysts.

In this study, TiO<sub>2</sub>@SiO<sub>2</sub> with core-shell structure was synthesized

\* Corresponding authors at: Faculty of Environmental Science and Engineering, Kunming University of Science and Technology, Kunming 650500, China.  
E-mail addresses: [likaikmust@163.com](mailto:likaikmust@163.com) (K. Li), [ningpingkmust@163.com](mailto:ningpingkmust@163.com) (P. Ning), [wangfei@kust.edu.cn](mailto:wangfei@kust.edu.cn) (F. Wang).

<sup>1</sup> C. W. and Z. L. contributed equally to this paper.

by classic Stöber process. Then, we prepared Ag-based catalysts using  $\text{TiO}_2$ ,  $\text{TiO}_2@\text{SiO}_2$ , and  $\text{SiO}_2$  as supports and evaluated their activities in the  $\text{NH}_3$ -SCO reaction. We observed that the support of Ag-based catalysts has a significant influence on the anchoring states of Ag, and the Ag/ $\text{TiO}_2@\text{SiO}_2$  catalyst exhibited much higher apparent and intrinsic activity than that of Ag/ $\text{TiO}_2$  and Ag/ $\text{SiO}_2$  catalysts. Characterization techniques and density functional theory (DFT) calculations elucidated that OH groups are the direct anchoring site of Ag on these supports, and the content and anchoring strength of OH groups on these supports together determine the anchoring states of Ag. Through the modulate of  $\text{SiO}_2$  encapsulation, Ag species were exclusively existed as  $\text{Ag}^0$  states and well dispersed on  $\text{TiO}_2@\text{SiO}_2$  due to the large numbers of OH groups with moderate anchoring strength, thus showing excellent  $\text{NH}_3$ -SCO performance. In addition, we studied the reaction mechanisms by the *in situ* diffuse reflection infrared Fourier transform spectrum (DRIFTS) analysis and the results showed that different reaction mechanisms appeared on these catalysts due to differences in Ag states.

## 2. Experimental

### 2.1. Materials preparation

#### 2.1.1. Materials

$\text{TiO}_2$  (anatase),  $\text{SiO}_2$ , tetraethyl orthosilicate (TEOS), and hexadecyl trimethyl ammonium bromide (CTAB) were purchased from Shanghai Aladdin Biochemical Technology Co., Ltd. Silver nitrate ( $\text{AgNO}_3$ ) was purchased from Alfa Aesar. Ethanol and aqueous ammonia ( $\text{NH}_3\cdot\text{H}_2\text{O}$ ) were supplied by Tianjin Zhiyuan Chemical Reagent Co., Ltd. All the materials were without further treatment. Deionized  $\text{H}_2\text{O}$  was used in the experiments.

#### 2.1.2. Preparation of $\text{TiO}_2@\text{SiO}_2$

$\text{SiO}_2$  encapsulated  $\text{TiO}_2$  powder was synthesized by classic Stöber process. First, 0.5 g of  $\text{TiO}_2$  powder was dissolved in ethanol (50 mL), after stirred for 30 min, and added  $\text{NH}_3\cdot\text{H}_2\text{O}$  drop by drop until the pH was 9.0. Then, 0.1 g of CTAB was added to the above solution and stirred well. Next, 0.2 mL of TEOS was added to the mixed solutions dropwise and stirred for 24 h at room temperature. Finally, the solid was collected by centrifugation and washed with alternating ethanol and deionized water for 3–5 times, and then dried in an oven at  $100^\circ\text{C}$  for 12 h. The dried solid designated as  $\text{TiO}_2@\text{SiO}_2$ .

#### 2.1.3. Preparation of catalysts

Ag/ $\text{TiO}_2$ , Ag/ $\text{TiO}_2@\text{SiO}_2$ , and Ag/ $\text{SiO}_2$  catalysts were prepared by co-impregnation of  $\text{TiO}_2$ ,  $\text{TiO}_2@\text{SiO}_2$ , and  $\text{SiO}_2$  powder with aqueous  $\text{AgNO}_3$ , with Ag loadings of 5 wt%. After stirring for 2 h at room temperature, the mixed solutions were added into a rotary evaporator to removal excess water. Then, the samples were dried at  $105^\circ\text{C}$  for 12 h and calcined in air for 3 h at  $450^\circ\text{C}$  afterwards, denoted as Ag/ $\text{TiO}_2$ , Ag/ $\text{TiO}_2@\text{SiO}_2$ , and Ag/ $\text{SiO}_2$ . The catalysts with 10 wt% Ag loadings were prepared as above and were denoted as 10Ag/ $\text{TiO}_2$ , 10Ag/ $\text{TiO}_2@\text{SiO}_2$ , and 10Ag/ $\text{SiO}_2$ . The catalysts were sieved to 40–60 mesh powders for testing.

### 2.2. Catalytic performance evaluation

The  $\text{NH}_3$ -SCO performance over the catalysts (50 mg) were performed in a fixed bed quartz tubular reactor with feed gas composed of 500 ppm of  $\text{NH}_3$ , 10 %  $\text{O}_2$ , 10 %  $\text{H}_2\text{O}$  (when used), and  $\text{N}_2$  balance; the total flow rate of the reaction mixture was  $100\text{ mL}\cdot\text{min}^{-1}$  with a gas hourly space velocity (GHSV) was  $136,000\text{ h}^{-1}$ . The stability test and cycling experiments were carried out under the same reaction conditions. The CO oxidation performance were performed in the above reactor with feed gas composed of 1 % CO, 10 %  $\text{O}_2$  and  $\text{N}_2$  balance. The concentrations of  $\text{NH}_3$ , NO,  $\text{NO}_2$ ,  $\text{N}_2\text{O}$ , and CO were monitored online by FTIR spectrometer (Nicolet iS 50) equipped with a deuterated triglycine

sulfate (DTGS) detector. The  $\text{NH}_3$  conversion,  $\text{N}_2$  selectivity, and CO conversion are defined in formulas (1), (2), and (3), respectively.

$$\text{NH}_3 \text{ Conversion} = \frac{[\text{NH}_3]_{\text{in}} - [\text{NH}_3]_{\text{out}}}{[\text{NH}_3]_{\text{in}}} \times 100 \% \quad (1)$$

$$\text{N}_2 \text{ Selectivity} = \left( 1 - \frac{2[\text{N}_2\text{O}]_{\text{out}} + [\text{NO}_2]_{\text{out}} + [\text{NO}]_{\text{out}}}{[\text{NH}_3]_{\text{in}} - [\text{NH}_3]_{\text{out}}} \right) \times 100 \% \quad (2)$$

$$\text{CO Conversion} = \frac{[\text{CO}]_{\text{in}} - [\text{CO}]_{\text{out}}}{[\text{CO}]_{\text{in}}} \times 100 \% \quad (3)$$

Kinetic experiments of  $\text{NH}_3$ -SCO were conducted in the above reactor. The activation energy ( $E_a$ ) was determined from the slope of Arrhenius plot (formula 4), in which  $\text{NH}_3$  conversion was controlled below 20 % to eliminate diffusion effects via varying the GHSV, as follow:

$$k = A \exp(E_a/RT) \quad (4)$$

and the k was calculated by the following formula (5):

$$k = -\frac{Q}{m} \ln(1 - \eta) \quad (5)$$

Where Q is the total gas flow ( $\text{mL}\cdot\text{min}^{-1}$ ), m is the catalyst weight (g), and  $\eta$  is the  $\text{NH}_3$  conversion (%).

Turnover frequencies (TOFs) were calculated according to formula (6):

$$\text{TOF} = \frac{\eta_{(\text{NH}_3)} \cdot Q / (60 \cdot V_m)}{(m \cdot w_{\text{Ag}} \cdot D_{\text{Ag}}) / M_{\text{Ag}}} \quad (6)$$

Where  $\eta_{(\text{NH}_3)}$ , Q,  $V_m$ , m,  $M_{\text{Ag}}$ , and  $w_{\text{Ag}}$  represent the  $\text{NH}_3$  conversion (%), the total flow rate ( $\text{L}\cdot\text{min}^{-1}$ ), molar volume of gas ( $22.4\text{ L}\cdot\text{mol}^{-1}$ ), the catalyst weight (g), silver molar mass ( $\text{g}\cdot\text{mol}^{-1}$ ), and Ag loadings (%), respectively.  $D_{\text{Ag}}$  is Ag dispersion calculated according to  $D_{\text{Ag}} = 1.31/d$ , in which d is the average size of Ag NPs measured by high-angle annular dark-field scanning transmission electron microscopy (HAADF-STEM).

The  $\text{O}_2$  reaction orders were measured by varying the  $\text{O}_2$  concentration from 6 % to 12 % with the  $\text{NH}_3$  concentration maintained at 500 ppm. And the  $\text{NH}_3$  reaction orders were evaluated by varying the  $\text{NH}_3$  concentration from 400 ppm to 800 ppm with the  $\text{O}_2$  concentration maintained at 10 %.

### 2.3. Catalyst characterization

Brunauer-Emmett-Teller (BET) analysis was performed on a physical adsorption instrument (NOVA 2000e) to obtain the surface areas and pore size distributions of catalysts. Powder X-ray diffraction (XRD) measurement was carried out on a computerized diffractometer (D8 ADVANCE, Bruker) with a  $\text{Cu K}\alpha$  radiation source (40 kV, 40 mA), XRD data were recorded over the  $2\theta$  range from  $20^\circ$  to  $80^\circ$  at a scan rate of  $5^\circ\cdot\text{min}^{-1}$ . High-resolution transmission electron microscopy (HRTEM) and HAADF-STEM images were performed with a FEI TalosF200x instrument, and an acceleration energy of 200 kV was applied. The X-ray Photoelectron Spectroscopy (XPS) analysis was performed using Al  $\text{K}\alpha$  radiation (Thermo fisher Scientific K-alpha) with the energy of the Al target power was at 72 W. The content of Si in  $\text{TiO}_2@\text{SiO}_2$  and the Ag loadings of catalysts were determined by inductively coupled plasma optical emission spectroscopy (ICP-OES). The  $\text{NH}_3$ -TPD experiments were performed on a Micromeritics AutoChem II 2920 instrument, 50 mg samples were pretreated at  $400^\circ\text{C}$  for 60 min with 20 %  $\text{O}_2/\text{N}_2$  ( $40\text{ mL}\cdot\text{min}^{-1}$ ) and cooled to  $50^\circ\text{C}$ . After purging with Ar for 30 min and then exposed to 2500 ppm  $\text{NH}_3/\text{N}_2$  for 60 min at  $50^\circ\text{C}$ . Then, the chamber was purged with  $\text{N}_2$  for 30 min and the temperature was increased to  $500^\circ\text{C}$  at a heating rate of  $10^\circ\text{C}\cdot\text{min}^{-1}$ .

Ag K-edge X-ray absorption fine structure (XAFS) measurements

were conducted at the BL01B1 beamline at Spring-8 (Harima Science Garden City, Hyogo) operated at 8 GeV using a Si (311) two-crystal monochromator. All spectra were acquired in under transmission mode at room temperature. The XAFS data were processed to isolate extended XAFS (EXAFS) and X-ray absorption near-edge structure (XANES) spectra from the background using Athena software. The filtered  $k^3$ -weighted  $\chi(k)$  was Fourier-transformed into R space using Artemis software. X-band electron paramagnetic resonance (EPR) measurements were performed on a Bruker EMXPLUS spectrometer.

Vacuum FTIR spectroscopy was used to detect the content of OH groups over samples. Firstly, the vacuum cell was kept under vacuum conditions at 400 °C for 1 h and then cooled down to 50 °C to collect the background spectra. 40 mg of a flaky sample was pretreated at 400 °C under vacuum conditions for 1 h, and collected the spectra when the temperature cooled down to 50 °C. *In situ* DRIFTS was conducted to investigate the reaction mechanism. The results were recorded using a FTIR spectrometer equipped with a liquid N<sub>2</sub> cooled MCT/A detector. The samples were firstly pretreated at 400 °C in 20 % O<sub>2</sub>/N<sub>2</sub> flow for 30 min, and cooled down to desired temperature (30–220 °C) in N<sub>2</sub> flow to collect the background spectra. Then, after 500 ppm of NH<sub>3</sub>/N<sub>2</sub> (100 mL·min<sup>-1</sup>) was introduced for 30 min, and N<sub>2</sub> purging at various temperatures to collect the NH<sub>3</sub> adsorption (at 30 °C) and desorption (30–220 °C) spectra. Next, the samples were pre-adsorbed with NH<sub>3</sub> (500 ppm) at 210 °C for 30 min and purged with N<sub>2</sub> for 15 min, and then O<sub>2</sub> (10 % in N<sub>2</sub>) was introduced to *in situ* cell to react for 30 min. Finally, cut off O<sub>2</sub> flow and reintroduced NH<sub>3</sub> flow for another 20 min. All spectra were averaged over accumulating 64 scans with a resolution of 4 cm<sup>-1</sup>.

## 2.4. DFT calculations

The adsorption energies in this study were performed in the framework of the DFT with the projector augmented plane-wave method, as implemented in the Vienna ab initio simulation package (VASP 5.4.4) [25,26]. The generalized gradient approximation proposed by Perdew-Burke-Ernzerhof (PBE), is selected for the exchange-correlation potential [27,28]. The cut-off energy for a plane wave is set to 450 eV during the calculations. The energy criterion is set to 10<sup>-5</sup> eV in the iterative solution of the Kohn-Sham equation. Structures were optimized until the residual forces on the atoms have declined to less than 0.02 eV/Å, and a 1 × 1 × 1 k-point grid was adopted based on the Monkhorst-Pack method. The bottom two layers were kept fixed and other atoms were fully relaxed, and a 15 Å vacuum region was used to avoid the periodic image interaction normal to the surface. The absorbed energy between TiO<sub>2</sub> (110) surface, TiO<sub>2</sub>@SiO<sub>2</sub> surface, SiO<sub>2</sub> (100) surface, and Ag atom were defined as following formula:

$$E_{\text{ad}} = E_{\text{total}} - E_{\text{surface}} - E_{\text{Ag}} \quad (7)$$

Where  $E_{\text{total}}$  is the total energies of the adsorbed system,  $E_{\text{surface}}$  is the energies of TiO<sub>2</sub> (110) surface, TiO<sub>2</sub>@SiO<sub>2</sub> surface, and SiO<sub>2</sub> (100) surface,  $E_{\text{Ag}}$  is the energy of an Ag atom.

## 3. Results

### 3.1. Structural features of supports

Energy dispersive spectrometer (EDS) and wide-survey XPS spectra were displayed in Fig. S1 and S2a, showing that Si element was successfully loaded onto TiO<sub>2</sub>. ICP-OES results show the mass fraction of Si atom on TiO<sub>2</sub>@SiO<sub>2</sub> is ca. 4.5 wt% (Table S1). As shown in Fig. S2b, compared with the TiO<sub>2</sub>, a new peak (centered at 532.9 eV) was observed on the O 1s XPS spectra of TiO<sub>2</sub>@SiO<sub>2</sub> and SiO<sub>2</sub>, corresponding to the O<sub>latt(Si)</sub> (lattice oxygen on SiO<sub>2</sub>), indicating that the Si element existed on TiO<sub>2</sub>@SiO<sub>2</sub> in the form of SiO<sub>2</sub>. In addition, the peak intensity of O<sub>latt(Ti)</sub> (lattice oxygen on TiO<sub>2</sub>) decreased significantly after

added SiO<sub>2</sub>, and lower than that of O<sub>latt(Si)</sub>, speculating that the SiO<sub>2</sub> might encapsulated on the surface of TiO<sub>2</sub> particles. From the HRTEM images of TiO<sub>2</sub> and TiO<sub>2</sub>@SiO<sub>2</sub> (Fig. S3), it can be seen that the addition of SiO<sub>2</sub> did not change the size and morphology of particles. Obvious diffraction peaks of TiO<sub>2</sub> rutile phase and SiO<sub>2</sub> were observed on TiO<sub>2</sub> (JCPDS 21–1276) and SiO<sub>2</sub> (JCPDS 29–0085) in XRD patterns (Fig. S4), respectively. However, no diffraction peak of SiO<sub>2</sub> appeared on TiO<sub>2</sub>@SiO<sub>2</sub> except for those of rutile phase, which might be due to the lower content of SiO<sub>2</sub>. It is worth noting that in Fig. 1a and e, the contour of TiO<sub>2</sub> particles is clear, in comparison, the TiO<sub>2</sub>@SiO<sub>2</sub> particles are blurred in outline and wrapped by a thin layer. EDS mapping and line scanning were used to further reveal the SiO<sub>2</sub> encapsulation layer, and the results present in Figs. 1b–d and 1f–h. The signal of Si elements was observed in the EDS mapping and line scanning images of TiO<sub>2</sub>@SiO<sub>2</sub>, and more Si elements and stronger Si signal appeared at the edge of particle (Fig. 1f and h), which is the typical feature of core-shell structure. Therefore, these above results confirmed that TiO<sub>2</sub> particles were encapsulated by SiO<sub>2</sub> layer, a TiO<sub>2</sub>@SiO<sub>2</sub> sample with core-shell structure was successfully synthesized. Next, we prepared catalysts by loaded 5 wt% Ag on TiO<sub>2</sub>, TiO<sub>2</sub>@SiO<sub>2</sub>, and SiO<sub>2</sub>, respectively, and evaluated their NH<sub>3</sub>-SCO performance.

### 3.2. NH<sub>3</sub>-SCO performance of catalysts

The NH<sub>3</sub>-SCO performance of catalysts is shown in Fig. 2a, the Ag/TiO<sub>2</sub>@SiO<sub>2</sub> catalyst showed higher NH<sub>3</sub> conversion than Ag/TiO<sub>2</sub> and Ag/SiO<sub>2</sub> at low temperature, and achieved T<sub>100</sub> (the temperature of 100 % conversion) at 200 °C. In contrast, the T<sub>100</sub> of Ag/TiO<sub>2</sub> and Ag/SiO<sub>2</sub> were as high as 250 °C and 275 °C, respectively. The Ag/TiO<sub>2</sub>@SiO<sub>2</sub> and Ag/SiO<sub>2</sub> catalysts possess a lower N<sub>2</sub> selectivity in comparison to Ag/TiO<sub>2</sub> (Fig. S5a), which was due to the generation of more N<sub>2</sub>O (Fig. S5b–d). The TOFs of catalysts were presented in form of histogram in Fig. 2b, the results revealed that the TOF of Ag/TiO<sub>2</sub>@SiO<sub>2</sub> was almost 9 times higher than that of Ag/TiO<sub>2</sub> and slightly higher than that of Ag/SiO<sub>2</sub>. In addition, kinetic measurements were performed and Arrhenius plots are shown in Fig. 2c, the E<sub>a</sub> on Ag/TiO<sub>2</sub>@SiO<sub>2</sub> (81.1 kJ·mol<sup>-1</sup>) was lower in comparison to Ag/TiO<sub>2</sub> (85.3 kJ·mol<sup>-1</sup>) and Ag/SiO<sub>2</sub> (92.5 kJ·mol<sup>-1</sup>).

The effect of water vapor in practical applications cannot be ignored, the water resistance tests of these catalysts were conducted and results were presented in Fig. S6. In the presence of 10 % H<sub>2</sub>O within the first 4 h, the activity of Ag/TiO<sub>2</sub> and Ag/TiO<sub>2</sub>@SiO<sub>2</sub> catalysts decreased to a similar extent, and returns to 100 % immediately after removal of H<sub>2</sub>O. With the continued introduction of H<sub>2</sub>O for another 4 h, the NH<sub>3</sub> conversion and N<sub>2</sub> selectivity of Ag/TiO<sub>2</sub>@SiO<sub>2</sub> catalyst were still maintained at around 86 % and 40 %, respectively. However, the NH<sub>3</sub> conversion of the Ag/TiO<sub>2</sub> catalyst sharply decreased to 20 % and the N<sub>2</sub> selectivity dropped to 0 %. The NH<sub>3</sub> conversion of the Ag/SiO<sub>2</sub> catalyst decreased to less than 20 % activity after the introduction of water. The long-term tests were conducted to evaluate the stability of these catalysts and the results shown in Fig. S7. The NH<sub>3</sub> conversion of Ag/TiO<sub>2</sub> and Ag/TiO<sub>2</sub>@SiO<sub>2</sub> catalysts remained constant throughout the process, while that of Ag/SiO<sub>2</sub> catalyst gradually decreased by about 15 %. It is noteworthy that, under the same Ag loading condition, differences in catalysts performance could be attributed to variations in the size and valence state of Ag species resulting from the metal-support interactions. In summary, in terms of performance, water resistance, and stability, the TiO<sub>2</sub>@SiO<sub>2</sub> has obvious advantages as the support of Ag-based catalyst for NH<sub>3</sub>-SCO.

### 3.3. States of Ag species on catalysts

We then performed comparative investigations of the Ag states over these catalysts using HAADF-STEM, XRD, and XAFS. Representative HAADF-STEM images in Fig. 3a–c display the dispersion of Ag particles of these catalysts. The size distribution of Ag particles on both Ag/TiO<sub>2</sub>

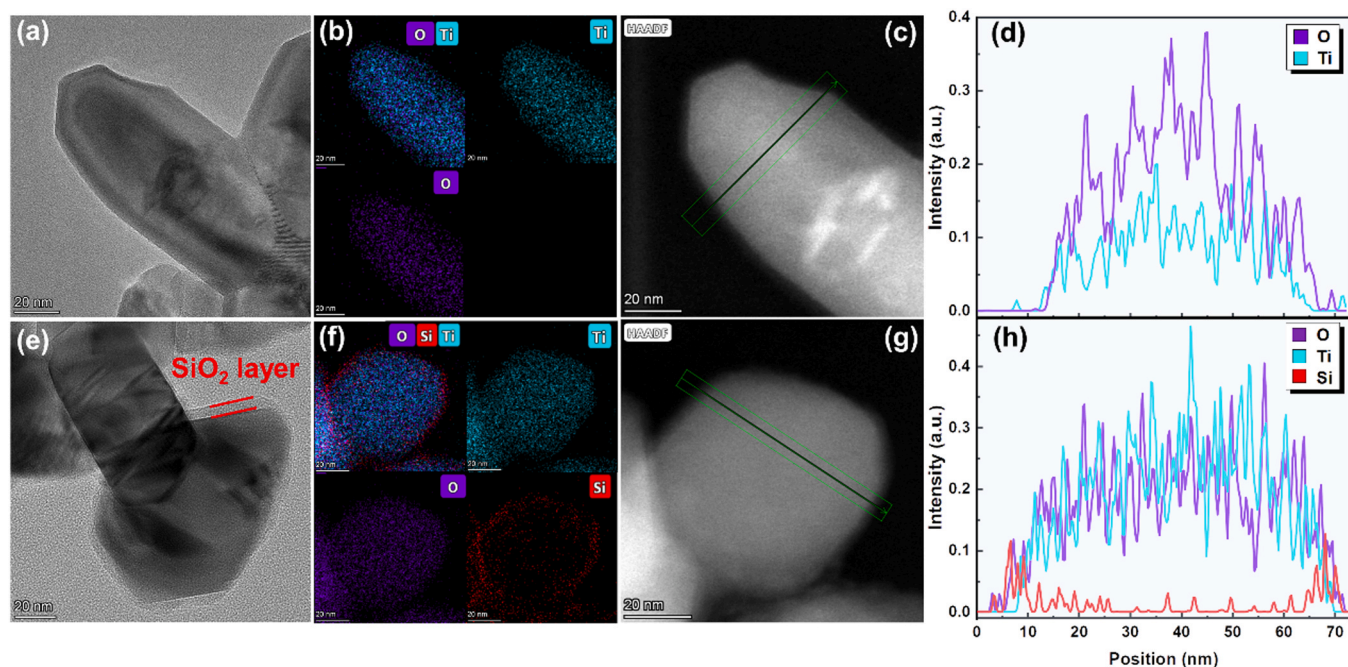


Fig. 1. (a) TEM image, (b) EDS mapping images (Ti, O), (c) line scanning image, and (d) line scanning pattern of  $\text{TiO}_2$  particle; (e) TEM image, (f) EDS mapping images (Ti, O, Si), (g) line scanning image, and (h) line scanning pattern of  $\text{TiO}_2/\text{SiO}_2$  particle.

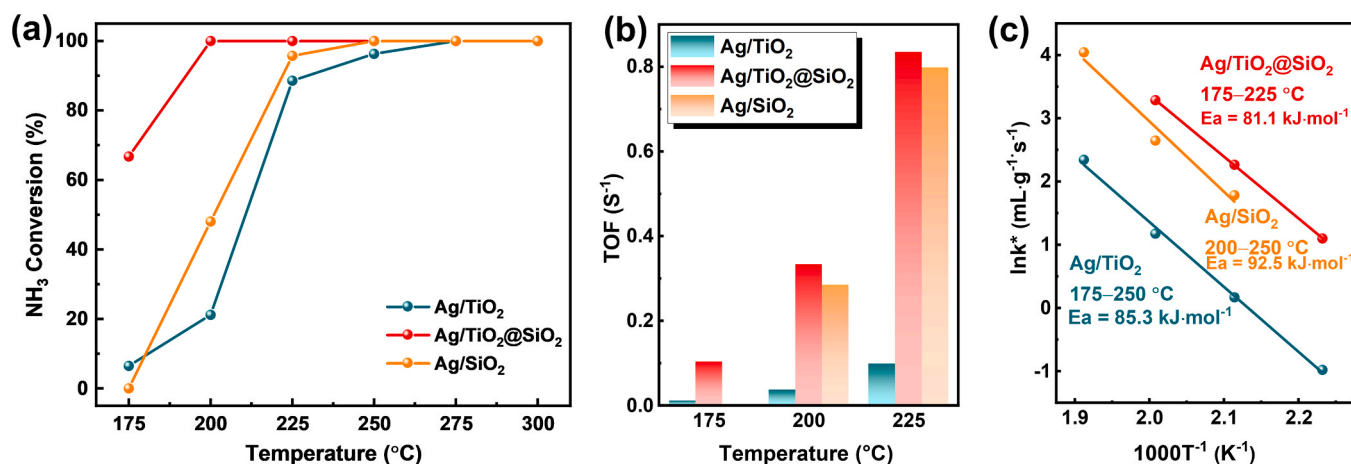


Fig. 2. (a)  $\text{NH}_3$  conversion, (b) TOFs, and (c) Arrhenius plots and corresponding  $E_a$  over catalysts. Reaction condition: 500 ppm  $\text{NH}_3$ , 10 %  $\text{O}_2$  in  $\text{N}_2$ , and GHSV =  $136,000 \text{ h}^{-1}$ .

and  $\text{Ag}/\text{SiO}_2$  was non-uniform. In detail, highly dispersed Ag NPs with the size is 1–2 nm predominated on  $\text{Ag}/\text{TiO}_2$ , and the 3–4 nm size of Ag NPs on  $\text{Ag}/\text{SiO}_2$  are mostly, as well as the simultaneous presence of large Ag NPs on both two catalysts. In contrast, uniform and well dispersed Ag NPs were observed on  $\text{Ag}/\text{TiO}_2/\text{SiO}_2$  without large aggregates, and the histograms of particle size distribution (insets in Fig. 3a–c) revealed that the average Ag particle sizes of  $\text{Ag}/\text{TiO}_2/\text{SiO}_2$  (2.8 nm) is smaller than  $\text{Ag}/\text{TiO}_2$  (2.9 nm) and  $\text{Ag}/\text{SiO}_2$  (4.6 nm). In addition, the corresponding HRTEM images (Fig. 3d–e) show that only a lattice spacing of 0.236 nm attributed to  $\text{Ag}^0$  (111) was measured on the three catalysts [20,29], and no lattice spacing of  $\text{Ag}_2\text{O}$  was observed possibly due to a lack of  $\text{Ag}_2\text{O}$  or in highly dispersed form. In the XRD patterns shown in Figs. 4a and 4b, diffraction peaks at  $38.1^\circ$ ,  $44.3^\circ$ , and  $64.5^\circ$  were detected in  $\text{Ag}/\text{TiO}_2$  and  $\text{Ag}/\text{SiO}_2$ , corresponding to (111), (200), and (220) lattice planes of  $\text{Ag}^0$  (JCPDS 87–0717), and the peak intensity of  $\text{Ag}^0$  on  $\text{Ag}/\text{SiO}_2$  is significantly higher than that on  $\text{Ag}/\text{TiO}_2$ . However, noticeable  $\text{Ag}^0$  reflections were not detected in case of  $\text{Ag}/\text{TiO}_2/\text{SiO}_2$ , indicating the

Ag species were well dispersed on  $\text{Ag}/\text{TiO}_2/\text{SiO}_2$ . In addition, No  $\text{Ag}_2\text{O}$  diffraction peaks were observed in the patterns of all catalysts, mainly due to a lack of  $\text{Ag}_2\text{O}$  or the small size of  $\text{Ag}_2\text{O}$  below the detection limit of XRD. This result is good agreement with the HRTEM observations.

The Ag-K edge XAFS measurements were performed to study the valence state and coordination environment of Ag species on those catalysts. XANES spectra showed that the white lines of the  $\text{Ag}/\text{TiO}_2$  closely resembled that of the  $\text{Ag}_2\text{O}$  reference, while the shape and absorption edge energy of  $\text{Ag}/\text{TiO}_2/\text{SiO}_2$  and  $\text{Ag}/\text{SiO}_2$  were quite similar with those of the Ag foil (Fig. 4c). This means that Ag species on  $\text{Ag}/\text{TiO}_2$  primarily existed in the oxidized state, while those on  $\text{Ag}/\text{TiO}_2/\text{SiO}_2$  and  $\text{Ag}/\text{SiO}_2$  were more predominantly in  $\text{Ag}^0$  [16,30]. As shown in Fig. 4d, two peaks at ca. 1.70 Å and ca. 2.67 Å were observed in the EXAFS spectra of the  $\text{Ag}/\text{TiO}_2$  catalyst, which were attributed to the Ag-O and Ag-Ag shells [31,32], respectively. However, only a strong Ag-Ag coordination shell at ca. 2.67 Å appeared on  $\text{Ag}/\text{TiO}_2/\text{SiO}_2$  and  $\text{Ag}/\text{SiO}_2$ . The fitting results of EXAFS were summarized in Table S2 (the



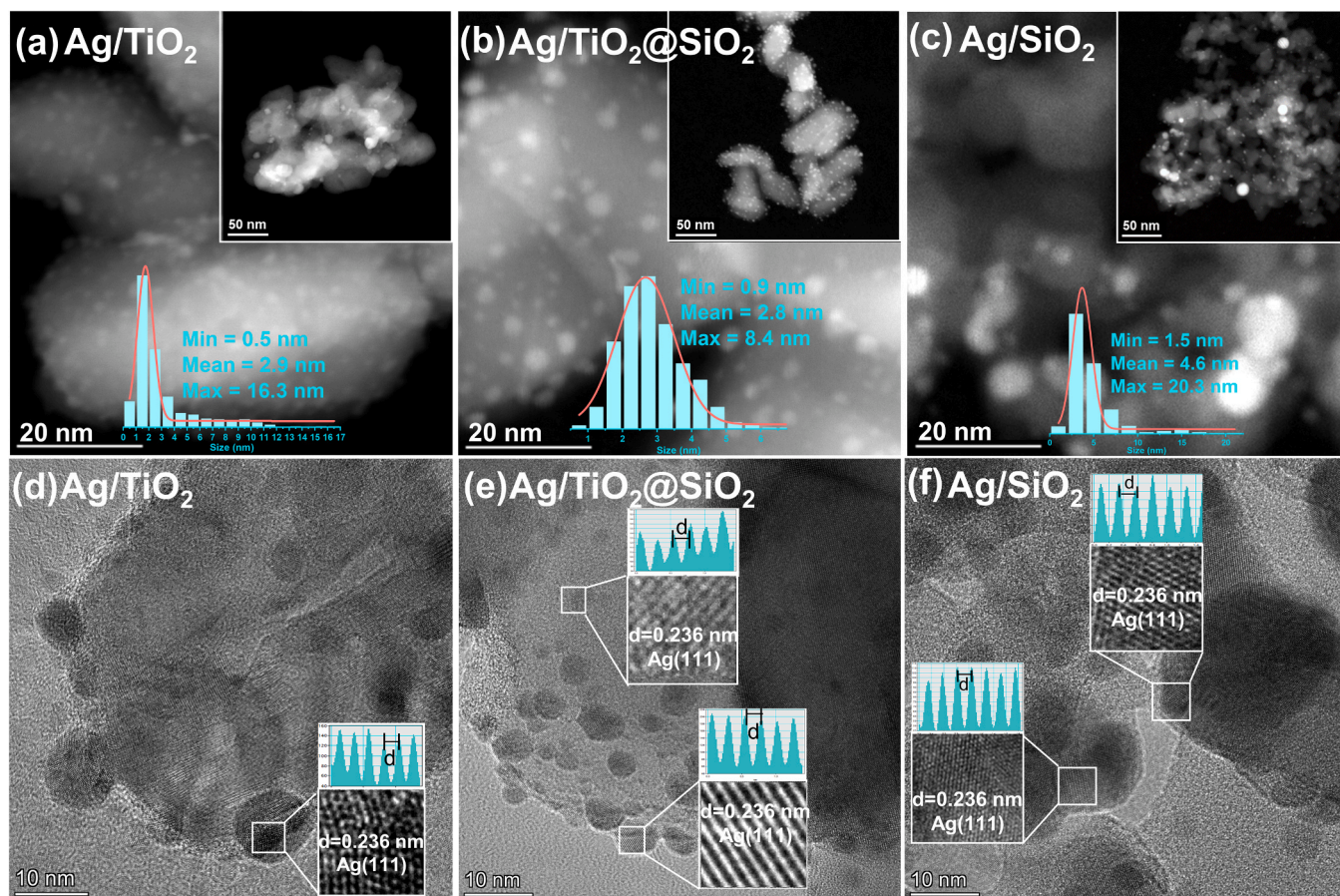


Fig. 3. HAADF-STEM images of (a) Ag/TiO<sub>2</sub>, (b) Ag/TiO<sub>2</sub>@SiO<sub>2</sub>, and (c) Ag/SiO<sub>2</sub>; corresponding HRTEM images of (d) Ag/TiO<sub>2</sub>, (e) Ag/TiO<sub>2</sub>@SiO<sub>2</sub>, and (f) Ag/SiO<sub>2</sub>.

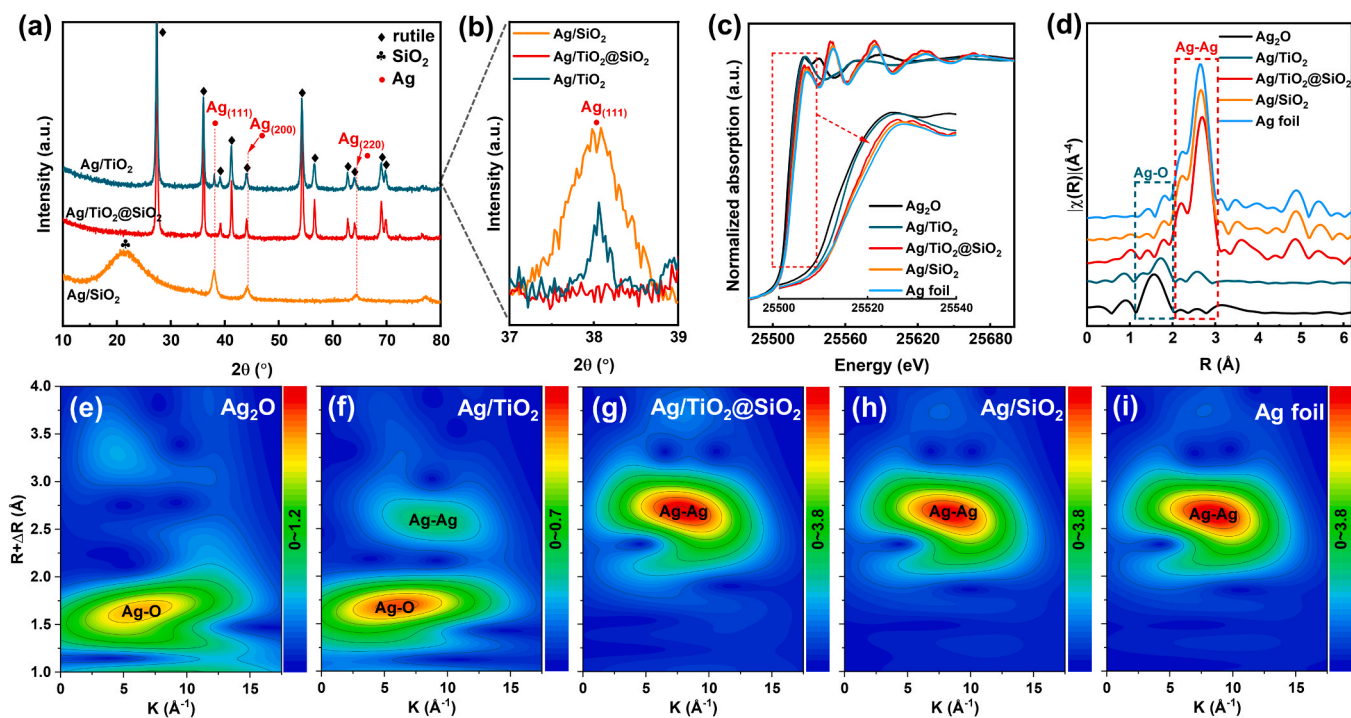


Fig. 4. (a) Wide range (10°–80°) and (b) narrow range (37°–39°) of XRD patterns; (c) Ag-K edge XANES and (d) EXAFS spectra of standard samples and catalysts; (e–i) wavelet transforms for Ag<sub>2</sub>O standard, Ag/TiO<sub>2</sub>, Ag/TiO<sub>2</sub>@SiO<sub>2</sub>, Ag/SiO<sub>2</sub>, and Ag foil.

fitting parameters and curves are shown in Fig. S8 and 9), the coordination number of Ag-O on Ag/TiO<sub>2</sub> (1.7) was near to that of Ag<sub>2</sub>O sample (2.1), and accompanied by a small amount of Ag-Ag coordination (0.6). However, only Ag-Ag coordination was presented on Ag/TiO<sub>2</sub>@SiO<sub>2</sub> and Ag/SiO<sub>2</sub>, and the bond distance and coordination number of them (2.86 Å, 10.5 for Ag/TiO<sub>2</sub>@SiO<sub>2</sub> and 2.86 Å, 11.8 for Ag/SiO<sub>2</sub>, respectively) were closer to Ag foil (2.86 Å and 12). As can be seen from the wavelet transform (WT) contour plots (Fig. 4e–i), two WT intensity maxima were observed over Ag/TiO<sub>2</sub>: one around at 1.60–1.80 Å assigned to the Ag-O coordination shell, another weak signal at 2.40–2.90 Å assigned to the Ag-Ag coordination shell. In contrast, only one WT maximum due to the Ag-Ag coordination shell presented on Ag/TiO<sub>2</sub>@SiO<sub>2</sub> and Ag/SiO<sub>2</sub>, which was quite similar to that of Ag foil. Accordingly, it is reasonable to conclude that a predominance of oxidized Ag species on Ag/TiO<sub>2</sub>, whereas all Ag species existed on Ag/TiO<sub>2</sub>@SiO<sub>2</sub> and Ag/SiO<sub>2</sub> in the form of Ag<sup>0</sup> NPs, and the size of Ag<sup>0</sup> NPs on Ag/SiO<sub>2</sub> is larger than that on Ag/TiO<sub>2</sub>@SiO<sub>2</sub> due to higher coordination numbers.

From the above experimental and characterization results, Ag species on Ag/TiO<sub>2</sub> is dominated by small size of Ag<sub>2</sub>O NPs and accompanied with a few large Ag<sup>0</sup> NPs. As previously reported, Ag<sup>0</sup> is the main active site of NH<sub>3</sub>-SCO reaction at low temperature [18]. Thus, Ag/TiO<sub>2</sub> has poor apparent and intrinsic activity due to lack of active sites. All Ag species highly dispersed on Ag/TiO<sub>2</sub>@SiO<sub>2</sub> samples in the form of Ag<sup>0</sup>, demonstrating superior apparent and intrinsic activity in NH<sub>3</sub>-SCO. Similar intrinsic activity was obtained on Ag/SiO<sub>2</sub> compared to Ag/TiO<sub>2</sub>@SiO<sub>2</sub>, while excessively large Ag<sup>0</sup> NPs accordingly reduced the concentrations of surface-active sites, thereby lowering the apparent activity.

### 3.4. The modulation mechanism of SiO<sub>2</sub>

Encapsulating SiO<sub>2</sub> on TiO<sub>2</sub> can effectively modulate the dispersion and valence states of Ag, thus improving the NH<sub>3</sub>-SCO activity. The states of Ag species on supported catalysts is normally linked to the interactions between Ag and support [33], which is typically determined by the anchoring sites on support. Therefore, we systematically compared the anchoring states on those three supports to investigate the intrinsic mechanism of the SiO<sub>2</sub> encapsulation modulating Ag states. Several previous studies mentioned that the dispersion of metals could be influenced by the specific surface area of support. As shown in Fig. S10, the smallest dispersion of Ag was observed on SiO<sub>2</sub> support with the largest specific surface area, thus, the effect of the specific surface area of the supports on the Ag states could be excluded.

The OH groups or defects (oxygen vacancy) on the surface of support have been reported to anchor metal atom [34–36]. According to previous investigations, metal atom is anchored by forming oxygen bridges with the oxygen of OH groups [34,36–38], or by coordinating with metals atoms near oxygen vacancy [39,40]. Xu et al. confirmed that the OH groups on rutile TiO<sub>2</sub> support is the anchoring sites of Ir single-atoms [37]. In this work, DFT calculations were conducted to determine the direct anchoring sites of Ag on these supports. Before the DFT calculations, the OH groups and oxygen vacancies contents on these supports were assessed and presented in Fig. S11. The FTIR spectra was shown in Fig. S11a, the peaks located in the range of 3500–3800 cm<sup>−1</sup> represent OH groups [41,42]. A signal of oxygen vacancy at  $g = 2.005$  were observed on the EPR spectra (Fig. S11b) [39,43], it can be seen that the TiO<sub>2</sub> support has the most oxygen vacancies and the fewest OH groups, while the opposite on the SiO<sub>2</sub> support. Thus, TiO<sub>2</sub> and SiO<sub>2</sub> supports were chosen for DFT calculations, and the results show that in the case of coexistence of OH groups and O vacancies (Fig. S12), Ag atom preferred to bond with the O atom of OH groups rather than supplement the O vacancies on TiO<sub>2</sub> and SiO<sub>2</sub> surface (Fig. S13). In addition, the content of OH groups on three samples exhibited a decreasing trend as the Ag loadings was increased from 1 to 5 wt% (Fig. S14a–c), and an obvious linear correlation between Ag loadings and OH group consumption was

observed on Fig. S15. Therefore, these results confirmed that OH groups are the direct anchoring sites of Ag on those supports.

As well known that the content of anchoring sites (OH groups) plays an important role in the anchoring states (valence and dispersion) of Ag species. The Ag dispersion and OH groups content on these supports are presented in Fig. S16, and no apparent linear relationship between them was observed, suggesting that the content of OH groups is not the only factor determining the anchoring states of Ag on the catalysts. As we can see from the optimized structures of the three supports (Fig. S17), the introduction of SiO<sub>2</sub> layer result in a reconfiguration of the overall structure, making the OH groups on TiO<sub>2</sub>@SiO<sub>2</sub> might be different from TiO<sub>2</sub>-OH and SiO<sub>2</sub>-OH. We speculate that differences in the anchoring strength of Ag on these three types of OH groups may be another important factor for influencing the anchoring states of Ag. Thus, the adsorption energies of Ag on these OH groups were calculated to compare the anchoring strength, and the results presented on Fig. 5a–c. On the surface of TiO<sub>2</sub>, Ag atom tended to coordinate two OH groups with a strong adsorption energy of −2.77 eV. However, Ag atom was only anchored to one OH group attached to Si atom on the SiO<sub>2</sub> model surfaces with an adsorption energy of −0.22 eV. The adsorption energy of Ag on TiO<sub>2</sub>@SiO<sub>2</sub> surface was −0.89 eV, between that on TiO<sub>2</sub> and SiO<sub>2</sub> models. A remarkable difference in anchoring strength of Ag on the different types of OH groups were also confirmed by differential charge density and Bader charge analysis. As shown in Fig. 5d–f, the electrons were transferred from Ag to the supports along the oxygen bridge (Ag-O bond) on the three structures, the numbers of electrons transferred from Ag to TiO<sub>2</sub>@SiO<sub>2</sub> (0.61 e<sup>−</sup>) were also between those of TiO<sub>2</sub> (0.82 e<sup>−</sup>) and SiO<sub>2</sub> (0.21 e<sup>−</sup>), indicating that the SiO<sub>2</sub> encapsulation successfully modulated the anchoring strength of OH groups.

From the above experimental and theoretical calculation results, we conclude that OH groups are the direct anchoring sites of Ag on supports, and the anchoring sites (OH groups) contents and the anchoring strength are together determined the valence and dispersion of Ag. In detail, On the TiO<sub>2</sub> surface with lower OH groups and strong anchoring strength, the Ag anchored on TiO<sub>2</sub>-OH can remain its dispersion with oxidized state during the high temperature calcination, whereas the other insufficient anchored of Ag tended to agglomerate into large Ag<sup>0</sup> NPs, thus showing an inhomogeneous and predominantly oxidized dispersion on TiO<sub>2</sub> surface. Although the SiO<sub>2</sub> surface with an abundant OH groups, due to the weaker anchoring strengths of SiO<sub>2</sub>-OH, the Ag-O bond was susceptible to break under high temperature and led to excessive agglomeration of Ag into large particles. The content and anchoring strength of OH groups on TiO<sub>2</sub>@SiO<sub>2</sub> are intermediate between the TiO<sub>2</sub> and SiO<sub>2</sub>, and abundant OH groups with moderate anchoring strength promote the formation of highly dispersed Ag<sup>0</sup> NPs on TiO<sub>2</sub>@SiO<sub>2</sub>, which is the active center of NH<sub>3</sub>-SCO.

### 3.5. Reaction mechanism

According to the N<sub>2</sub> selectivity, by-product analysis, and kinetic experiment results, the reaction mechanisms of Ag/TiO<sub>2</sub>@SiO<sub>2</sub> and Ag/SiO<sub>2</sub> in NH<sub>3</sub>-SCO are consistent, while different from that of AgTiO<sub>2</sub>. It is well known that OH groups, acting as Brønsted acid sites, can adsorb NH<sub>3</sub> to some extent, which may affect the NH<sub>3</sub>-SCO performance of catalysts. In the NH<sub>3</sub>-TPD experiments conducted (Fig. S18), we observed that the NH<sub>3</sub> desorption peaks of Ag/TiO<sub>2</sub>, Ag/TiO<sub>2</sub>@SiO<sub>2</sub>, and Ag/SiO<sub>2</sub> catalysts all appeared below 400 °C, with intensities lower than those of TiO<sub>2</sub>, TiO<sub>2</sub>@SiO<sub>2</sub>, and SiO<sub>2</sub> supports, respectively. This suggests that OH groups both anchoring Ag and serve as weak to medium acid sites for NH<sub>3</sub> adsorption. It is worth noting that among the three catalysts, the Ag/TiO<sub>2</sub> exhibited the highest NH<sub>3</sub> adsorption capacity, yet it did not demonstrate the best NH<sub>3</sub>-SCO performance. This indicates that NH<sub>3</sub> adsorption induced by OH groups are not the key factor determining the NH<sub>3</sub>-SCO performance of these catalysts. Then, the O<sub>2</sub> and NH<sub>3</sub> reaction orders were evaluated for further identification of rate-determining factors. As shown in Fig. S19, the O<sub>2</sub> reaction orders were



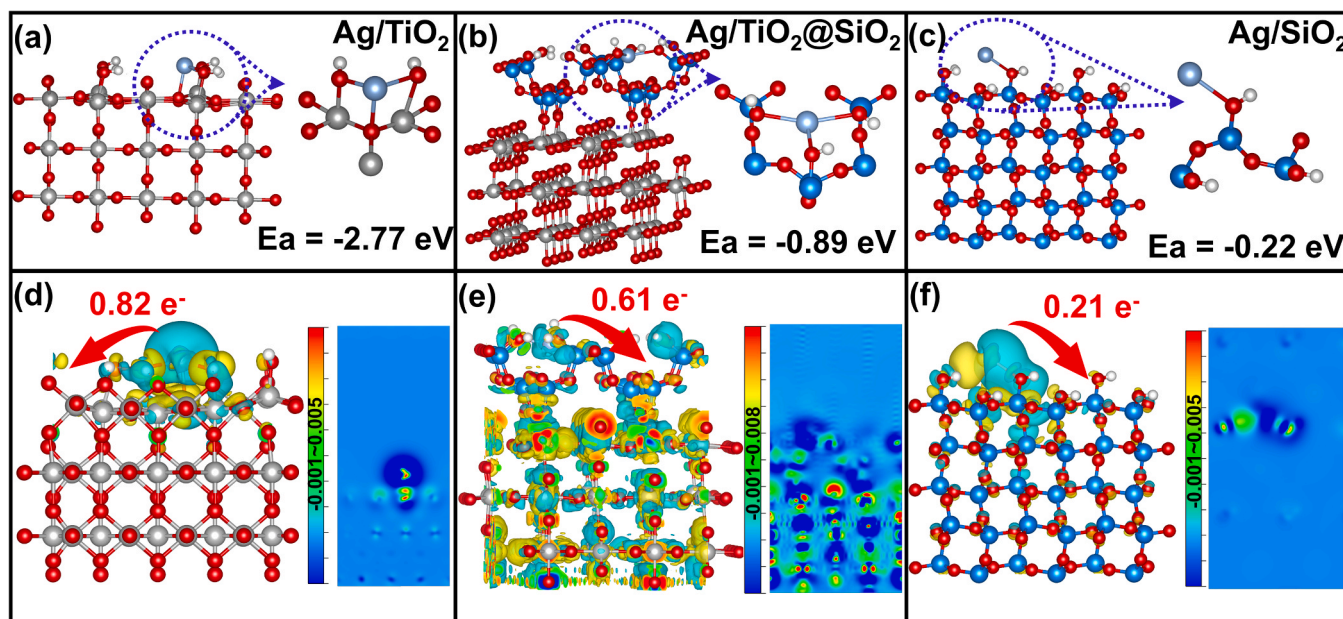


**Fig. 5.** Optimized geometries and binding energies of Ag adsorbed on (a)  $\text{TiO}_2$  (110) surface, (b)  $\text{TiO}_2/\text{SiO}_2$  surface, and (c)  $\text{SiO}_2$  (100) surface (grey: Ti atom, blue: Si atom, red: O atom, white: H atom, silvery: Ag atom); corresponding charge density difference of Ag adsorbed on (d)  $\text{TiO}_2$  (110), (e)  $\text{TiO}_2/\text{SiO}_2$ , and (f)  $\text{SiO}_2$  (100), where the yellow and cyan regions represent the electron accumulation and depletion, respectively.

higher than the  $\text{NH}_3$  reaction orders of these catalysts, indicating that  $\text{O}_2$  activation capacity plays a more essential role than  $\text{NH}_3$  adsorption on these catalysts in  $\text{NH}_3$ -SCO reactions. Besides, the  $\text{O}_2$  reaction orders of  $\text{Ag}/\text{TiO}_2/\text{SiO}_2$  and  $\text{Ag}/\text{SiO}_2$  catalysts was almost three times higher than that of  $\text{Ag}/\text{TiO}_2$  catalyst. It can be concluded that differences in  $\text{O}_2$  activation capacity due to Ag states are the rate-determining factors and underlying reason for distinct in reaction mechanisms.

Therefore, the specific reaction behaviors of pre-adsorbed  $\text{NH}_3$  and  $\text{O}_2$  on  $\text{Ag}/\text{TiO}_2$  and  $\text{Ag}/\text{TiO}_2/\text{SiO}_2$  was studied by *in situ* DRIFTS. Fig. S20a and c shows the *in situ* DRIFTS of  $\text{NH}_3$  adsorption on  $\text{Ag}/\text{TiO}_2$ , the vibrations of  $\text{NH}_3$  coordinated on Lewis acid sites (1162, 1200, and  $1600\text{ cm}^{-1}$ ) and  $\text{NH}_4^+$  bonded to Brønsted acid sites (1324, 1380, and

$1470\text{ cm}^{-1}$ ) [22,44,45] were observed. In addition, the band located at  $1560\text{ cm}^{-1}$  was ascribed to  $-\text{NH}_2$  stretching vibration modes [17,46], and the band at  $1430\text{ cm}^{-1}$  was attributed to  $-\text{NH}$  were also detected [45,47], indicating  $\text{NH}_3$  could be dissociated at room temperature due to the large  $\text{Ag}^0$  NPs on  $\text{Ag}/\text{TiO}_2$ . As the temperature increased, the bands of ionic  $\text{NH}_4^+$  and coordinated  $\text{NH}_3$  quickly decreased (Fig. 6a and e), and the bands of  $-\text{NH}_2$  and  $-\text{NH}$  increased in intensity. In addition, two new bands were ascribed to  $-\text{HNO}$  ( $1529\text{ cm}^{-1}$ ) [17] and  $\text{NH}_2-\text{NH}_2$  ( $1456\text{ cm}^{-1}$ ) [19] appeared and grew gradually. It was reported that the  $-\text{NH}$  and  $-\text{HNO}$  are the key intermediates of the imide ( $-\text{NH}$ ) mechanism [17]. The *in situ* DRIFTS spectra of the reaction between  $\text{O}_2$  and pre-adsorbed  $\text{NH}_3$  at  $210^\circ\text{C}$  is shown in Fig. 6b and f, the  $-\text{NH}_2$  and

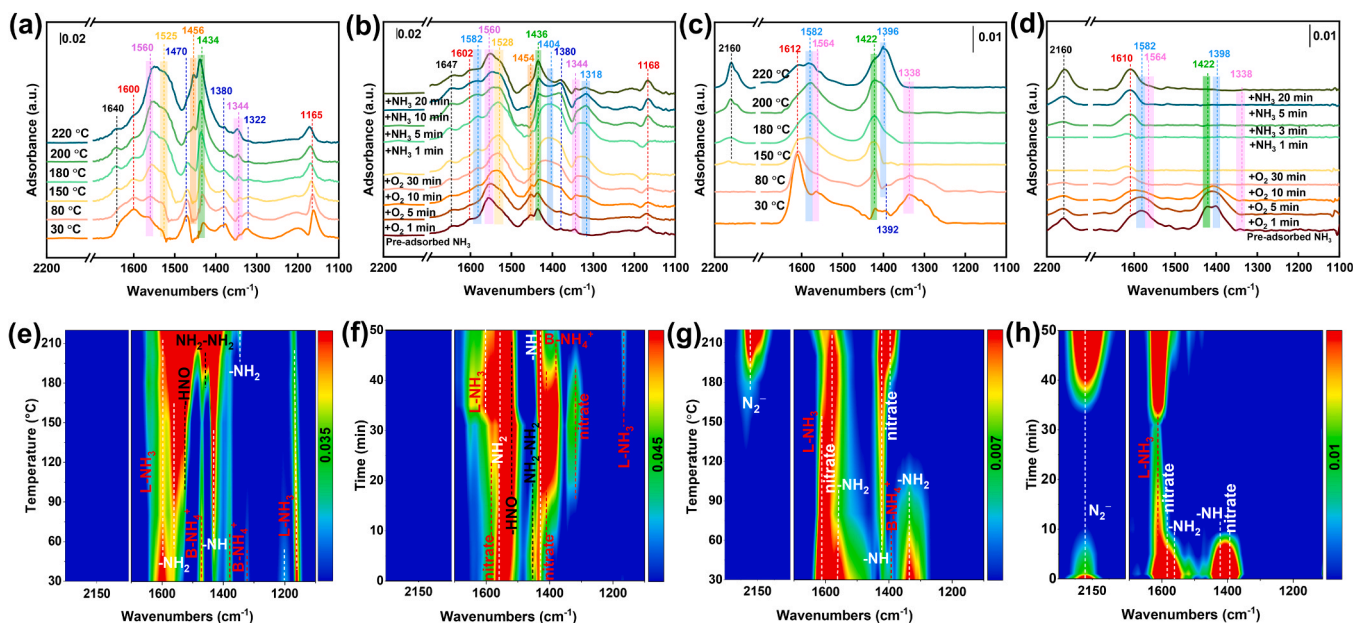


**Fig. 6.** *In situ* DRIFTS results over samples. (a) and (c)  $\text{NH}_3$  desorption at various temperatures after  $\text{N}_2$  purging at  $30^\circ\text{C}$ , (b) and (e) reaction between  $\text{O}_2$  and pre-adsorbed  $\text{NH}_3$  species at  $210^\circ\text{C}$  and further reaction with  $\text{NH}_3$  over  $\text{Ag}/\text{TiO}_2$  and  $\text{Ag}/\text{TiO}_2/\text{SiO}_2$ . (e), (f), (g) and (h) are contour maps corresponding to (a), (b), (c), and (d), respectively. Reaction conditions: 500 ppm  $\text{NH}_3$ , 10 %  $\text{O}_2$  in  $\text{N}_2$ .

–NH consumed rapidly with the introduction of O<sub>2</sub>, and more –HNO generated. In the same time, new bands assigned to nitrate (1318, 1404, and 1582 cm<sup>−1</sup>) [22,45,48,49] were appeared, which could be attributed to the action of Ag<sub>2</sub>O under oxygen-enriched conditions. When O<sub>2</sub> was cut off and NH<sub>3</sub> reintroduced, the nitrate quickly reacted with NH<sub>3</sub> and consumed, and the NH<sub>3</sub> adsorptions and intermediates reappeared. This process was consistent the typical i-SCR mechanism as be reported [21,44]. Overall, the reaction pathway on Ag/TiO<sub>2</sub> followed both –NH and i-SCR mechanisms.

*In situ* DRIFTS of NH<sub>3</sub> adsorption at 30 °C on Ag/TiO<sub>2</sub>@SiO<sub>2</sub> are shown in Fig. S20b and d, the bands located at 1612 cm<sup>−1</sup> and 1394 cm<sup>−1</sup> related to the ammonia species on Lewis and Brønsted acid sites, respectively, and the bands of –NH<sub>2</sub> (1564 and 1338 cm<sup>−1</sup>) and –NH (1422 cm<sup>−1</sup>) were also detected. As shown in Fig. 6c and g, the bands of ammonia species on acid sites and the –NH<sub>2</sub> rapidly disappeared with an increase in temperature, while the intensity of –NH band increased. Interestingly, new bands ascribed to nitrate (1398 and 1582 cm<sup>−1</sup>) [48,50] and N<sub>2</sub><sup>−</sup> species (2160 cm<sup>−1</sup>) [17,21] appeared at higher temperatures. The nitrate could be produced by the –NH<sub>x</sub> (–NH<sub>2</sub> or –NH) interacted with lattice oxygen at higher temperatures [51], and then the *in situ*-formed nitrate further combined with –NH<sub>x</sub> and reduced into N<sub>2</sub><sup>−</sup> species [17]. After O<sub>2</sub> was introduced into system (Fig. 6d and h), all peaks decreased rapidly. The N<sub>2</sub><sup>−</sup> species could be desorbed into N<sub>2</sub> [16,21], or easily interacted with molecular O<sub>2</sub> and converted into N<sub>2</sub>O [21], thus, more N<sub>2</sub>O was observed from by-product analysis shown in Fig. S5c, and the N<sub>2</sub> selectivity of Ag/TiO<sub>2</sub>@SiO<sub>2</sub> catalyst was relatively lower than that of Ag/TiO<sub>2</sub>.

#### 4. Discussion

In the present work, TiO<sub>2</sub>@SiO<sub>2</sub> support with core-shell structure was prepared by classic Stöber method, then, we used a facile impregnation method to synthesis the Ag/TiO<sub>2</sub>, Ag/TiO<sub>2</sub>@SiO<sub>2</sub>, and Ag/SiO<sub>2</sub> catalysts. The HAADF-STEM, XRD, and XAFS analysis of those catalysts shown that the states of Ag species on the three supports are significantly different. Previous studies have reported that Ag<sup>0</sup> species are the main active center for the NH<sub>3</sub>-SCO reaction, whereas Ag<sup>+</sup> species only exhibit certain activity at high temperatures [18]. The Ag species on Ag/TiO<sub>2</sub>@SiO<sub>2</sub> are completely existed as highly dispersed Ag<sup>0</sup> NPs, thus, exhibiting superior apparent and intrinsic activity in NH<sub>3</sub>-SCO. Many studies have shown that the metal states on supported catalysts are determined by the anchoring sites on the supports. Xu et al. demonstrated that the OH groups on vacancy-deficient rutile TiO<sub>2</sub> is a key site for determining the dispersion and morphology of Ir species [37]. However, these studies mainly focus on revealing that the content of OH groups on the same supports affects the metal anchoring states [34,37,52,53]. In this work, for the different supports, besides the content of OH groups, we found that the anchoring strength of OH groups also play an important role in determining the anchoring states of Ag. Experiments and DFT calculations revealed that the content of OH groups on TiO<sub>2</sub> is much lower than that on SiO<sub>2</sub>, but the anchoring strength of OH groups for Ag on TiO<sub>2</sub> is much higher than that on SiO<sub>2</sub>. The introduction of SiO<sub>2</sub> layer on TiO<sub>2</sub> successfully modulated the OH groups content and anchoring strength, contributing to the formation of abundant OH groups with moderate anchoring strengths on TiO<sub>2</sub>@SiO<sub>2</sub>. The cycling experiments were conducted and the results shown that there was no change in activity of Ag/TiO<sub>2</sub> catalyst due to the strong anchoring strength, a slight decrease in the activity of the Ag/TiO<sub>2</sub>@SiO<sub>2</sub> catalyst in the third cycle, whereas the activity of the weaker anchored Ag/SiO<sub>2</sub> samples decreased drastically in the second cycle (Fig. S21). These cycling results also verified the differences in anchoring strength of OH groups on the three supports and well agreed with the DFT results. Our study demonstrated the content of OH groups and its anchoring strength jointly determine the anchoring state of Ag species, and the OH groups content and its anchoring strength on TiO<sub>2</sub> were successfully modulated by the introduction of SiO<sub>2</sub> layer. Then, we loaded 10 wt% Ag on these

three supports for CO catalytic oxidation, and the low-temperature activity of 10Ag/TiO<sub>2</sub>@SiO<sub>2</sub> catalyst was also significantly better than that of 10Ag/TiO<sub>2</sub> and 10Ag/SiO<sub>2</sub> catalysts (Fig. S22), which confirmed that our findings can be generalized to other oxidation reactions.

As we known, the states of Ag significantly affect the activation capacity of oxygen, which in turn may influence the reaction pathway and catalytic performance [21,30]. Similarly, significant differences in NH<sub>3</sub>-SCO reaction mechanisms were found on Ag/TiO<sub>2</sub> dominated by Ag<sup>+</sup> species and Ag/TiO<sub>2</sub>@SiO<sub>2</sub> and Ag/SiO<sub>2</sub> with exclusively Ag<sup>0</sup> species. The *in situ* DRIFTS analysis of Ag/TiO<sub>2</sub> catalyst shown that the key intermediates (–NH and –HNO) of the –NH mechanism was appeared with increasing temperature, as well as the nitrate species formed after the introduction of O<sub>2</sub> and disappeared when the reintroduction of NH<sub>3</sub>, indicating Ag/TiO<sub>2</sub> follows both the –NH and i-SCR mechanisms possibly due to the coexistence of Ag<sub>2</sub>O and Ag<sup>0</sup> NPs. For the Ag/TiO<sub>2</sub>@SiO<sub>2</sub>, the NH<sub>3</sub> was stepwise dissociated to –NH<sub>2</sub> and –NH in the action of Ag<sup>0</sup> NPs at room temperature, and further generated nitrate species at high temperature. The *in situ*-formed nitrate interacted with NH<sub>x</sub> to N<sub>2</sub><sup>−</sup> species, which was desorbed or reacted with molecular O<sub>2</sub> at high temperatures to form the final products (gaseous N<sub>2</sub> or N<sub>2</sub>O). Overall, inconsistent of reaction mechanism on Ag/TiO<sub>2</sub> and Ag/TiO<sub>2</sub>@SiO<sub>2</sub> led to differences NH<sub>3</sub>-SCO performance.

#### 5. Conclusions

In summary, we prepared TiO<sub>2</sub>@SiO<sub>2</sub> with a core-shell structure and used it as support to synthesis Ag/TiO<sub>2</sub>@SiO<sub>2</sub> catalyst. Compared with Ag/TiO<sub>2</sub> and Ag/SiO<sub>2</sub>, Ag/TiO<sub>2</sub>@SiO<sub>2</sub> catalyst exhibited superior apparent and intrinsic activities in NH<sub>3</sub>-SCO reaction. HAADF-STEM, XRD, and XAFS results revealed that more and well dispersed Ag<sup>0</sup> species formed on Ag/TiO<sub>2</sub>@SiO<sub>2</sub> catalyst. Based on experimental and DFT calculations analysis, it was confirmed that the OH groups are the direct anchoring sites of Ag on supports, and the content and anchoring strength of OH groups on these supports significantly determine the anchoring states of Ag. Benefiting from the modulation of SiO<sub>2</sub> layer, abundant OH groups with moderate anchoring strength facilitate the formation of highly dispersed Ag<sup>0</sup> species on TiO<sub>2</sub>@SiO<sub>2</sub>. Research on the NH<sub>3</sub>-SCO mechanism showed the different states of Ag on these catalysts lead to the differences of reaction pathway, more and well dispersed Ag<sup>0</sup> NPs on Ag/TiO<sub>2</sub>@SiO<sub>2</sub> were conducive to follow the mechanism with lower energy barriers in NH<sub>3</sub>-SCO reaction, thus exhibiting higher apparent and intrinsic activity. Our study systematically elucidates the modulation mechanism of the anchoring states of Ag on supported catalysts, providing new insight for the design of Ag-based catalyst with specific states.

#### CRedit authorship contribution statement

**Chunxue Wang:** Writing – original draft, Investigation, Data curation. **Zhao Li:** Writing – original draft, Software, Methodology. **Xin Sun:** Validation, Investigation. **Yuan Li:** Investigation, Data curation. **Lei Shi:** Validation, Resources. **Shunzheng Zhao:** Investigation, Conceptualization. **Kai Li:** Writing – original draft, Resources, Conceptualization. **Ping Ning:** Writing – review & editing, Supervision, Resources. **Fei Wang:** Writing – review & editing, Funding acquisition, Conceptualization.

#### Declaration of Competing Interest

The authors declare that they have no known competing financial interests or personal relationships that could have appeared to influence the work reported in this paper.

#### Data availability

Data will be made available on request.



## Acknowledgements

This work was financially supported by the National Natural Science Foundation of China (No. 52370113), Yunnan Fundamental Research Projects (Grant No. 202101BE070001-001), Yunnan Major Scientific and Technological Projects (Grant No. 202202AG050005).

## Appendix A. Supporting information

Supplementary data associated with this article can be found in the online version at [doi:10.1016/j.apcatb.2024.124091](https://doi.org/10.1016/j.apcatb.2024.124091).

## References

- [1] B. Gu, M.A. Sutton, S.X. Chang, Y. Ge, J. Chang, Agricultural ammonia emissions contribute to China's urban air pollution, *Front. Ecol. Environ.* 12 (2014) 265–266, <https://doi.org/10.1890/14.Wb.007>.
- [2] C. Huang, Q. Hu, S. Lou, J. Tian, R. Wang, C. Xu, J. An, H. Ren, D. Ma, Y. Quan, Y. Zhang, L. Li, Ammonia emission measurements for light-duty gasoline vehicles in china and implications for emission modeling, *Environ. Sci. Technol.* 52 (2018) 11223–11231, <https://doi.org/10.1021/acs.est.8b03984>.
- [3] Y. Pan, S. Tian, D. Liu, Y. Fang, X. Zhu, Q. Zhang, B. Zheng, G. Michalski, Y. Wang, Reply to comment on "fossil fuel combustion-related emissions dominate atmospheric ammonia sources during severe haze episodes: Evidence from (15)N-stable isotope in size-resolved aerosol ammonium, *Environ. Sci. Technol.* 50 (2016) 10767–10768, <https://doi.org/10.1021/acs.est.6b04197>.
- [4] L. Wang, X. Yu, Y. Wei, J. Liu, Z. Zhao, Research advances of rare earth catalysts for catalytic purification of vehicle exhausts-commemorating the 100th anniversary of the birth of Academician, *J. Rare Earths* (2021), <https://doi.org/10.1016/j.jre.2021.05.001>.
- [5] L. Kong, X. Tang, J. Zhu, Z. Wang, Y. Pan, H. Wu, L. Wu, Q. Wu, Y. He, S. Tian, Y. Xie, Z. Liu, W. Sui, L. Han, G. Carmichael, Improved inversion of monthly ammonia emissions in china based on the chinese ammonia monitoring network and ensemble kalman filter, *Environ. Sci. Technol.* 53 (2019) 12529–12538, <https://doi.org/10.1021/acs.est.9b02701>.
- [6] Y. Shu, J. Ji, M. Zhou, S. Liang, Q. Xie, S. Li, B. Liu, J. Deng, J. Cao, S. Liu, H. Huang, Selective photocatalytic oxidation of gaseous ammonia at ppb level over Pt and F modified TiO<sub>2</sub>, *Appl. Catal., B* 300 (2022), <https://doi.org/10.1016/j.apcatb.2021.120688>.
- [7] S. Chatterjee, R.K. Parsapur, K.-W. Huang, Limitations of ammonia as a hydrogen energy carrier for the transportation sector, *ACS Energy Lett.* 6 (2021) 4390–4394, <https://doi.org/10.1021/acsenenergylett.1c02189>.
- [8] A. Valera-Medina, F. Amer-Hatem, A.K. Azad, I.C. Dedoussi, M. de Joannon, R. X. Fernandes, P. Glarborg, H. Hashemi, X. He, S. Mashruk, J. McGowan, C. Mounaim-Rouselle, A. Ortiz-Prado, A. Ortiz-Valera, I. Rossetti, B. Shu, M. Yehia, H. Xiao, M. Costa, Review on ammonia as a potential fuel: from synthesis to economics, *Energy Fuels* 35 (2021) 6964–7029, <https://doi.org/10.1021/acs.energyfuels.0c03685>.
- [9] L. Chmielarz, M. Jabłońska, Advances in selective catalytic oxidation of ammonia to dinitrogen: a review, *RSC Adv.* 5 (2015) 43408–43431, <https://doi.org/10.1039/C5RA03218K>.
- [10] F. Gao, Y. Liu, Z. Sani, X. Tang, H. Yi, S. Zhao, Q. Yu, Y. Zhou, Advances in selective catalytic oxidation of ammonia (NH<sub>3</sub>-SCO) to dinitrogen in excess oxygen: a review on typical catalysts, catalytic performances and reaction mechanisms, *J. Environ. Chem. Eng.* 9 (2021), <https://doi.org/10.1016/j.jece.2020.104575>.
- [11] Y. Wang, W. Xu, C. Li, Y. Yang, Z. Geng, T. Zhu, Effects of IrO<sub>2</sub> nanoparticle sizes on Ir/Al<sub>2</sub>O<sub>3</sub> catalysts for the selective catalytic oxidation of ammonia, *Chem. Eng. J.* 437 (2022), <https://doi.org/10.1016/j.cej.2022.135398>.
- [12] T. Zhang, H. Chang, Y. You, C. Shi, J. Li, Excellent activity and selectivity of one-pot synthesized Cu-SSZ-13 catalyst in the selective catalytic oxidation of ammonia to nitrogen, *Environ. Sci. Technol.* 52 (2018) 4802–4808, <https://doi.org/10.1021/acs.est.8b00267>.
- [13] M. Jabłońska, A. Król, E. Kukulska-Zajac, K. Tarach, L. Chmielarz, K. Góra-Marek, Zeolite Y modified with palladium as effective catalyst for selective catalytic oxidation of ammonia to nitrogen, *J. Catal.* 316 (2014) 36–46, <https://doi.org/10.1016/j.jcat.2014.04.022>.
- [14] L. Chmielarz, P. Kuśtrowski, A. Rafalska-Lasocha, R. Dziembaj, Selective oxidation of ammonia to nitrogen on transition metal containing mixed metal oxides, *Appl. Catal., B* 58 (2005) 235–244, <https://doi.org/10.1016/j.apcatb.2004.12.009>.
- [15] W. Liu, Y. Long, X. Tong, Y. Yin, X. Li, J. Hu, Transition metals modified commercial SCR catalysts as efficient catalysts in NH<sub>3</sub>-SCO and NH<sub>3</sub>-SCR reactions, *Mol. Catal.* 515 (2021), <https://doi.org/10.1016/j.mcat.2021.111888>.
- [16] H. Wang, T. Murayama, M. Lin, N. Sakaguchi, M. Haruta, H. Miura, T. Shishido, Understanding the distinct effects of Ag nanoparticles and highly dispersed Ag species on N<sub>2</sub> selectivity in NH<sub>3</sub>-SCO reaction, *ACS Catal.* (2022) 6108–6118, <https://doi.org/10.1021/acscatal.1c05762>.
- [17] L. Zhang, H. He, Mechanism of selective catalytic oxidation of ammonia to nitrogen over Ag/Al<sub>2</sub>O<sub>3</sub>, *J. Catal.* 268 (2009) 18–25, <https://doi.org/10.1016/j.jcat.2009.08.011>.
- [18] L. Zhang, C. Zhang, H. He, The role of silver species on Ag/Al<sub>2</sub>O<sub>3</sub> catalysts for the selective catalytic oxidation of ammonia to nitrogen, *J. Catal.* 261 (2009) 101–109, <https://doi.org/10.1016/j.jcat.2008.11.004>.
- [19] G. Xu, Y. Zhang, J. Lin, Y. Wang, X. Shi, Y. Yu, H. He, Unraveling the mechanism of ammonia selective catalytic oxidation on Ag/Al<sub>2</sub>O<sub>3</sub> catalysts by operando spectroscopy, *ACS Catal.* 11 (2021) 5506–5516, <https://doi.org/10.1021/acscatal.1c01054>.
- [20] F. Wang, G. He, B. Zhang, M. Chen, X. Chen, C. Zhang, H. He, Insights into the activation effect of H<sub>2</sub> pretreatment on Ag/Al<sub>2</sub>O<sub>3</sub> catalyst for the selective oxidation of ammonia, *ACS Catal.* 9 (2019) 1437–1445, <https://doi.org/10.1021/acscatal.8b03744>.
- [21] F. Wang, J. Ma, G. He, M. Chen, C. Zhang, H. He, Nanosize effect of Al<sub>2</sub>O<sub>3</sub> in Ag/Al<sub>2</sub>O<sub>3</sub> catalyst for the selective catalytic oxidation of ammonia, *ACS Catal.* 8 (2018) 2670–2682, <https://doi.org/10.1021/acscatal.7b03799>.
- [22] F. Wang, J. Ma, G. He, M. Chen, S. Wang, C. Zhang, H. He, Synergistic effect of TiO<sub>2</sub>-SiO<sub>2</sub> in Ag/Si-Ti catalyst for the selective catalytic oxidation of ammonia, *Ind. Eng. Chem. Res.* 57 (2018) 11903–11910, <https://doi.org/10.1021/acs.iecr.8b02205>.
- [23] G. Corro, E. Vidal, S. Cebada, U. Pal, F. Bañuelos, D. Vargas, E. Guilleminot, Electronic state of silver in Ag/SiO<sub>2</sub> and Ag/ZnO catalysts and its effect on diesel particulate matter oxidation: An XPS study, *Appl. Catal., B* 216 (2017) 1–10, <https://doi.org/10.1016/j.apcatb.2017.05.059>.
- [24] V.V. Dutov, G.V. Mamontov, V.I. Zaikovskii, L.F. Liotta, O.V. Vodyankina, Low-temperature CO oxidation over Ag/SiO<sub>2</sub> catalysts: effect of OH/Ag ratio, *Appl. Catal., B* 221 (2018) 598–609, <https://doi.org/10.1016/j.apcatb.2017.09.051>.
- [25] J.P. Perdew, K. Burke, M. Ernzerhof, Generalized gradient approximation made simple, *Phys. Rev. Lett.* 77 (1996) 3865–3868, <https://doi.org/10.1103/PhysRevLett.77.3865>.
- [26] G. Kresse, J. Furthmüller, Efficient iterative schemes for ab initio total-energy calculations using a plane-wave basis set, *Phys. Rev. B* 54 (1996) 11169–11186, <https://doi.org/10.1103/PhysRevB.54.11169>.
- [27] R. Xiao, H. Li, L. Chen, High-throughput design and optimization of fast lithium ion conductors by the combination of bond-valence method and density functional theory, *Sci. Rep.* 5 (2015) 14227, <https://doi.org/10.1038/srep14227>.
- [28] D. Chen, X. Lei, Y. Wang, S. Zhong, G. Liu, B. Xu, C. Ouyang, Tunable electronic structures in BP/MoSSe van der Waals heterostructures by external electric field and strain, *Appl. Surf. Sci.* 497 (2019) 143809, <https://doi.org/10.1016/j.apsusc.2019.143809>.
- [29] X. Hu, Q. Zhu, X. Wang, N. Kawazoe, Y. Yang, Nonmetal-metal-semiconductor-promoted P/Ag/Ag<sub>2</sub>O/Ag<sub>3</sub>PO<sub>4</sub>/TiO<sub>2</sub> photocatalyst with superior photocatalytic activity and stability, *J. Mater. Chem. A* 3 (2015) 17858–17865, <https://doi.org/10.1039/C5TA05153C>.
- [30] F. Wang, Z. Li, H. Wang, M. Chen, C. Zhang, P. Ning, H. He, Nano-sized Ag rather than single-atom Ag determines CO oxidation activity and stability, *Nano Res.* 15 (2021) 452–456, <https://doi.org/10.1007/s12274-021-3501-1>.
- [31] Z. Li, J. Zhao, J. Gao, Y. Li, S. Bao, K. Li, P. Ning, F. Wang, Reduction-aggregation" strategy to construct a low-cost and high-efficiency Ag/Al<sub>2</sub>O<sub>3</sub> catalyst for NH<sub>3</sub>-SCO, *Sup. Purif. Technol.* 317 (2023), <https://doi.org/10.1016/j.seppur.2023.123881>.
- [32] H. Wang, M. Lin, T. Murayama, S. Feng, M. Haruta, H. Miura, T. Shishido, Ag size/structure-dependent effect on low-temperature selective catalytic oxidation of NH<sub>3</sub> over Ag/MnO<sub>2</sub>, *ACS Catal.* 11 (2021) 8576–8584, <https://doi.org/10.1021/acscatal.1c01130>.
- [33] Y. Li, H. He, C.B. Zhang, J. Zhang, M. Chen, Influence of alkali metals on Pd/TiO<sub>2</sub> catalysts for catalytic oxidation of formaldehyde at room temperature, *Catal. Sci. Technol.* (2016), <https://doi.org/10.1039/C5CY01521A>.
- [34] F. Wang, J. Ma, S. Xin, Q. Wang, J. Xu, C. Zhang, H. He, X. Cheng Zeng, Resolving the puzzle of single-atom silver dispersion on nanosized gamma-Al<sub>2</sub>O<sub>3</sub> surface for high catalytic performance, *Nat. Commun.* 11 (2020) 529, <https://doi.org/10.1038/s41467-019-13937-1>.
- [35] F. Kraushofer, L. Haager, M. Eder, A. Rafsanjani-Abbasi, Z. Jakub, G. Franceschi, M. Riva, M. Meier, M. Schmid, U. Diebold, G.S. Parkinson, Single Rh adatoms stabilized on  $\alpha$ -Fe<sub>2</sub>O<sub>3</sub>(11-02) by coadsorbed water, *ACS Energy Lett.* 7 (2022) 375–380, <https://doi.org/10.1021/acsenenergylett.1c02405>.
- [36] L. DeRita, J. Resasco, S. Dai, A. Boubnov, H.V. Thang, A.S. Hoffman, I. Ro, G. W. Graham, S.R. Bare, G. Pacchioni, X. Pan, P. Christopher, Structural evolution of atomically dispersed Pt catalysts dictates reactivity, *Nat. Mater.* (2019) 746–751, <https://doi.org/10.1038/s41563-019-0349-9>.
- [37] W. Xu, Y. Wang, H. He, J. Yang, Y. Yang, J. Ma, C. Li, T. Zhu, Insight into hydroxyl groups in anchoring Ir single-atoms on vacancy-deficient rutile TiO<sub>2</sub> supports for selective catalytic oxidation of ammonia, *Appl. Catal., B* 345 (2024), <https://doi.org/10.1016/j.apcatb.2023.123684>.
- [38] Y. Choi, G. Kim, J. Kim, S. Lee, J.-C. Kim, R. Ryoo, H. Lee, Anchoring catalytically active species on alumina via surface hydroxyl group for durable surface reaction, *Appl. Catal., B* 325 (2023), <https://doi.org/10.1016/j.apcatb.2022.122325>.
- [39] J. Wan, W. Chen, C. Jia, L. Zheng, J. Dong, X. Zheng, Y. Wang, W. Yan, C. Chen, Q. Peng, D. Wang, Y. Li, Defect effects on TiO<sub>2</sub> nanosheets: stabilizing single atomic site Au and promoting catalytic properties, *Adv. Mater.* 30 (2018), <https://doi.org/10.1002/adma.201705369>.
- [40] X. Liu, M.H. Liu, Y.C. Luo, C.Y. Mou, S.D. Lin, H. Cheng, J.M. Chen, J.F. Lee, T. S. Lin, Strong metal-support interactions between gold nanoparticles and ZnO nanorods in CO oxidation, *J. Am. Chem. Soc.* 134 (2012) 10251–10258, <https://doi.org/10.1021/ja3033235>.
- [41] Y. Hui, J. Zheng, Y. Qin, X. Du, Y. Zu, J. Yang, S. Sun, X. Gao, Z. Sun, L. Song, Insight into the nature and the transformation of the hydroxyl species in the CeY zeolite, *Inorganic Chemistry Frontiers*, <https://doi.org/10.1039/D1QI01564H>.
- [42] A. Mahdavi-Shakib, J.M.A. Ramos, R.N. Austin, T.J. Schwartz, B.G. Frederick, Frequencies and thermal stability of isolated surface hydroxyls on pyrogenic TiO<sub>2</sub>

- nanoparticles, *J. Phys. Chem. C* 123 (2019), <https://doi.org/10.1021/acs.jpcc.9b05699>.
- [43] Q. Zhang, D. Chen, Q. Song, C. Zhou, D. Li, D. Tian, D. Jiang, Holey defected TiO<sub>2</sub> nanosheets with oxygen vacancies for efficient photocatalytic hydrogen production from water splitting, *Surf. Interfaces* 23 (2021), <https://doi.org/10.1016/j.surfin.2021.100979>.
- [44] Y. Wang, W. Xu, X. Chen, C. Li, J. Xie, Y. Yang, T. Zhu, C. Zhang, Single-atom Ir<sub>1</sub> supported on rutile TiO<sub>2</sub> for excellent selective catalytic oxidation of ammonia, *J. Hazard. Mater.* 432 (2022) 128670, <https://doi.org/10.1016/j.jhazmat.2022.128670>.
- [45] H. Wang, P. Ning, Q. Zhang, X. Liu, T. Zhang, J. Fan, J. Wang, K. Long, Promotional mechanism of WO<sub>3</sub> over RuO<sub>2</sub>-Fe<sub>2</sub>O<sub>3</sub> catalyst for NH<sub>3</sub>-SCO reaction, *Appl. Catal. A* 561 (2018) 158–167, <https://doi.org/10.1016/j.apcata.2018.05.020>.
- [46] J.H. Shin, G.J. Kim, S.C. Hong, Reaction properties of ruthenium over Ru/TiO<sub>2</sub> for selective catalytic oxidation of ammonia to nitrogen, *Appl. Surf. Sci.* 506 (2020), <https://doi.org/10.1016/j.apsusc.2019.144906>.
- [47] E.K. Dann, E.K. Gibson, R.H. Blackmore, C.R.A. Catlow, P. Collier, A. Chutia, T. E. Erden, C. Hardacre, A. Kroner, M. Nachtegaal, A. Raj, S.M. Rogers, S.F.R. Taylor, P. Thompson, G.F. Tierney, C.D. Zeinalipour-Yazdi, A. Goguet, P.P. Wells, Structural selectivity of supported Pd nanoparticles for catalytic NH<sub>3</sub> oxidation resolved using combined operando spectroscopy, *Nat. Catal.* 2 (2019) 157–163, <https://doi.org/10.1038/s41929-018-0213-3>.
- [48] F. Cao, J. Xiang, S. Su, P. Wang, L. Sun, The activity and characterization of MnOx-CeO<sub>2</sub>-ZrO<sub>2</sub>/c-Al<sub>2</sub>O<sub>3</sub> catalysts for low temperature selective catalytic reduction of NO with NH<sub>3</sub>, *Chem. Eng. J. (Lausanne, Switz.)* (2014), <https://doi.org/10.1016/j.cej.2014.01.034>.
- [49] L. Xu, X.S. Li, M. Crocker, Z.S. Zhang, A.M. Zhu, C. Shi, A study of the mechanism of low-temperature SCR of NO with NH<sub>3</sub> on MnOx/CeO<sub>2</sub>, *J. Mol. Catal. A Chem.* 378 (2013) 82–90, <https://doi.org/10.1016/j.molcata.2013.05.021>.
- [50] Z. Zhang, R. Li, M. Wang, Y. Li, Y. Tong, P. Yang, Y. Zhu, Two steps synthesis of CeTiOx oxides nanotube catalyst: enhanced activity, resistance of SO<sub>2</sub> and H<sub>2</sub>O for low temperature NH<sub>3</sub>-SCR of NOx, *Appl. Catal., B* 282 (2021), <https://doi.org/10.1016/j.apcatb.2020.119542>.
- [51] Y. Liu, Z. Liu, C. Wang, J. Xu, J. Ai, X. Liu, A. Zhang, Y. Zhao, C. Du, B. Shan, Unraveling the lattice O assisted internal selective catalytic reduction mechanism on high N<sub>2</sub> selectivity of CuOx/PtCu catalysts in NH<sub>3</sub>-SCO, *ACS Catal.* 13 (2023) 7178–7188, <https://doi.org/10.1021/acscatal.3c00314>.
- [52] Y. Fan, F. Wang, R. Li, C. Liu, Q. Fu, Surface hydroxyl-determined migration and anchoring of silver on alumina in oxidative redispersion, *ACS Catal.* 13 (2023) 2277–2285, <https://doi.org/10.1021/acscatal.2c05453>.
- [53] F. Wang, K. Li, B. Li, C. Wang, Z. Li, Y. Zhang, W. Shan, Y. Yu, C. Zhang, Q. Fu, P. Ning, J.S. Francisco, X.C. Zeng, H. He, Identification of direct anchoring sites for monoatomic dispersion of precious metals (Pt, Pd, Ag) on CeO<sub>2</sub> support, *Angew. Chem. Int. Ed. Engl.* 63 (2024) e202318492, <https://doi.org/10.1002/anie.202318492>.